

Role of Electronic Excited State in Kinetics of the $\text{CH}_2\text{OO} + \text{SO}_2 \rightarrow \text{HCHO} + \text{SO}_3$ Reaction

Qingfei Song,^{1,2} Qiuyu Zhang,^{1,2,*} and Qingyong Meng^{1,2,†}

¹*Department of Chemistry, Northwestern Polytechnical University,
West Youyi Road 127, 710072 Xi'an, China*

²*Key Laboratory of Special Functional and Smart Polymer
Materials of Ministry of Industry and Information Technology,
Northwestern Polytechnical University,
West Youyi Road 127, 710072 Xi'an, China*

(Dated: March 7, 2021)

Abstract

In this work, kinetics of the $\text{CH}_2\text{OO} + \text{SO}_2 \rightarrow \text{HCHO} + \text{SO}_3$ reaction was studied by ring-polymer molecular dynamics (RPMD). To perform RPMD calculations, multi-reference configuration interaction (MRCI) was first carried out to compute data for constructing potential energy surface (PES) through a kernel regression method. On the basis of the present MRCI calculations, the statics multi-state mechanism involving the lowest-lying singlet excited state (denoted by S_1) was proposed, which is different from the previously proposed mechanism with the lowest-lying triplet state (denoted by T_1). Moreover, the present RPMD calculations predicted the rate coefficient of $3.95 \times 10^{-11} \text{ cm}^3 \text{ molecule}^{-1} \text{ s}^{-1}$ at the room temperature (namely 298 K), agreeing with the previously reported experimental values. Finally, based on the present calculations, a probable dynamics mechanism was discussed, where the produced HCHO molecule was proposed to be in a vibrationally excited state. This needs further experimental and theoretical observation in the future.

Keywords: *Kernel Regression Method; Potential Energy Surface; Rate Coefficient; $\text{CH}_2\text{OO} + \text{SO}_2$*

*Electronic address: qyzhang@nwpu.edu.cn

†Electronic address: qingyong.meng@nwpu.edu.cn

Although the simplest Criegee intermediate (CI), CH_2OO , was firstly postulated by Criegee in 1949, it was not directly detected until Welz *et al.* [1] reported the first experimental observation of CI. Since then, many experimental studies [2–11] of CIs reactivity were reported and clarified the important role of CH_2OO in the oxidation of SO_2 [11, 12], which produces SO_3 and subsequently H_2SO_4 . In 2012, Vereecken *et al.* [12] reported their mechanism of the $\text{CH}_2\text{OO} + \text{SO}_2 \rightarrow \text{HCHO} + \text{SO}_3$ reaction at the M05-2X/aug-cc-pVDZ level in 2012. As shown in Figure 6 of reference [12], they identified that, in the vicinity of the biradical adduct of CH_2OO and SO_2 , the singlet and triplet states are split by less than 0.4 kJ mol^{-1} , which implies singlet-triplet mixing may be significant and lead to reversible ISC in the mechanism at the near degeneracy there or elsewhere. With this idea in the mind to explain their cavity ring-down spectroscopy (CRDS) experiment, Chhantyal-Pun *et al.* [11] hypothesized an ISC mechanism or SO_2 -catalysed but reversible isomerization, in competition with the $\text{CH}_2\text{OO} + \text{SO}_2 \rightarrow \text{HCHO} + \text{SO}_3$ channel.

In this work, we study this multi-state mechanism through multireference *ab initio* calculations as well as quantum dynamics which requires a global potential energy surface (PES). First of all, this multi-state mechanism involving a triplet state [12] was originally proposed by the single-reference M05-2X method, which is not suitable for multi-state problem. And hence, multireference *ab initio* calculations are necessary. Second, to the best of our knowledge, there is still no quantum-dynamics studies on the kinetics of the title reaction in the literature. Here, we theoretically observe the rate coefficient of the $\text{CH}_2\text{OO} + \text{SO}_2 \rightarrow \text{HCHO} + \text{SO}_3$ reaction via ring-polymer molecular dynamics (RPMD) method [13–15] based on the PES fitted by kernel regression method, that is Gaussian process regression (GPR) algorithm [16, 17]. This algorithm is considered suitable for efficiently constructing high-dimensional PES through fewer energy points [16, 17]. In RPMD, the classical molecular dynamics, which is performed in an extended phase space with n -beads imaginary time path integral, is isomorphic to the path-integral quantum dynamics as $n \rightarrow \infty$. Studies on the polyatomic reactions, in particular the gas-phase reactions involving alkanes, clearly show its power [17–20].

Geometry and atom labeling used for the $\text{CH}_2\text{OO} + \text{SO}_2$ system are shown in Figure 1. In this work, coordinates for building PES consist of bond lengths, bond angles and dihedral angles, which are transferred to Cartesian coordinates in RPMD calculations. Because the system has no symmetry, in energy calculations for database, the electronic states are labeled using the irreducible representations in the C_1 group (namely A_1). During reaction process the CH_2OO fragment always constructs a plane, while the SO_2 molecule constructs another plane. These two planes are

shown by different background colors in Figure 1. In this work, these two planes will be always maintained. On the basis of the above coordinates, the multi-configurational self-consistent field (MCSCF) [21, 22] and multi-reference configuration interaction (MRCI) [21, 23] with the active space of $(8e, 6o)$, were carried out by MOLPRO version 2019.1 [24, 25] to determine the static mechanism and build the database for PES. The active space of $(8e, 6o)$ was also used for the MRCI study on the $\text{CH}_2\text{OO} + \text{O}_3 \rightarrow \text{HCHO} + 2\text{O}_2$ reaction. Since O_3 and SO_2 have the same number of valence electrons, we choose the $(8e, 6o)$ space as the active space in the present work. Further calculation details of MCSCF and MRCI are given in the Supporting Information. The results on the electronic states predicted the lower-lying electronic states of 1^1A , 1^3A , and 2^1A , which are denoted by S_0 , T_1 , and S_1 , respectively.

In construction of PES, we first computed the MRCI energies of the sampled points in relevant configurational space to build the database, and then fitted the database by a kernel regression method. To sample the points in configurational space, the weighted random sampling-grids were used in different regions to sample relevant points. Having built the database of electronic energies, the GPR algorithm was implemented. The reader is referred to references [16, 17] for details of GPR, which is also simply described in the Supporting Information. Here, only a description of model integration is given. As a kind of kernel regression method, when the amount of data exceeds some criteria, the inherent prohibitively high cost of GPR in training makes high-dimensional GPR PES expensive to use. A way to gain similar performance at a lower price is to combine several prediction models into one.

In this work, we constructed the GPR PES in the integration of models to incorporate inferences from difference resources and reduce the possibility of fatal failure originating from a sole model. Since GPR gives the uncertainty accompanied with prediction values, that is,

$$f_*|y \sim \mathcal{N}[\mathbf{K}_*^T(\mathbf{K} + \sigma^2\mathbf{I})^{-1}y, \mathbf{K}_{**} - \mathbf{K}_*^T(\mathbf{K} + \sigma^2\mathbf{I})^{-1}\mathbf{K}_*], \quad (1)$$

the weights of models can be derived from the ratio of uncertainties in different models. By means of Bayesian model averaging, the distribution of the combined value can be written as

$$p(x) = \sum_{k=1}^K \pi_k \mathcal{N}(x|\mu_k, \Sigma_k), \quad (2)$$

where K is the number of combined models, π_k are the Bayesian weights and μ_k , Σ_k are the parameters of individual models. Therefore, one can approximately give the final potential function

in the form [26]

$$\mathcal{E}(f_*) = \sum_{k=1}^K \pi_k \mu_k, \quad (3)$$

where $\mathcal{E}(f_*)$ is the posterior mean of the resulting potential energy. In this work, we considered three cases of equation (3) in GPR fitting processes. The first case is called the individual model, where $K = 1$. The second case is called direct integration model, where $\pi_k = 1/K$. The third case is the Bayesian integration model, where π_k has to be computed from single model uncertainty. On the basis of the PES given in equation (3), extensive RPMD calculations were performed to compute rate coefficient at 298 K. Details of the present RPMD calculations are given in the Supporting Information. Based on the present calculations, we can find several points as follows.

First of all, let us consider the statics mechanism of the title reaction. At a set of fixed $R(S - O)$ (see Figure 1) values ranging from 1.3 Å to 3.5 Å, the MRCI partial geometry optimization calculations for these states were performed. The potential energy curves (PECs) for the different states can be then drawn on the basis of the resulting MRCI energies. From these energy curves, one can find the nearly crossing points, based on which one has to further optimize the geometries of the S_0/S_1 and S_0/T_1 minimum-energy crossing point (MECP). Since the transition between S_0 and T_1 is forbidden by electron spin, to further determine the transitions probability, the spin-orbital coupling was also computed at geometry of the S_0/T_1 MECP. Moreover, since the reaction system belongs to the C_1 group, the transition between S_0 and S_1 is allowed by vibronic coupling according to the group-theory analysis. Illustrated in Figure 2 are PECs for the S_0 , S_1 , and T_1 states. We also qualitatively show the regions of the MECPs by a gray box. Based on these PECs, further geometry optimizations were performed for the MECPs. Given in Table I are the optimized geometries and energy differences for the S_0/S_1 and S_0/T_1 MECPs (see also Figures 2 and 3 of the Supporting Information), together with the assignments of the imaginary vibrational frequencies. Given in Table I of the Supporting Information are the MRCI electronic configurations, which clearly shows the multi-reference feature of the $\text{CH}_2\text{OO} + \text{SO}_2$ system.

The simplest process of the $\text{CH}_2\text{OO} + \text{SO}_2 \rightarrow \text{HCHO} + \text{SO}_3$ reaction is the translational process of the O atom from CH_2OO to SO_2 . Thus, the important parameters in the reaction process are bond lengths of S-O and O-O bonds contained in the reaction coordinate. Comparing these two bond lengths with the corresponding values of reactant and product, the S_0/S_1 and S_0/T_1 MECPs should locate at the reaction coordinate, which implies that the MECPs should be involved into the reaction process. The imaginary frequencies and their assignments of these MECPs clearly

show that the MECPs are close to the reaction coordinate but not strictly locate at it. The MRCI energies (relative to the reactant group) for the S_0/S_1 and S_0/T_1 MECPs are 2.20 eV and 8.10 eV, respectively. Although the vertical excitation energy of 1.81 eV for the T_1 state of CH_2OO is not too large (even smaller than the energy of the S_0/S_1 MECP), the high energy (8.10 eV) of the S_0/T_1 MECP as well as the spin-forbidden feature of the $T_1 \leftarrow S_0$ transition imply that triplet state might be hardly involved in the reaction mechanism. Moreover, the spin-orbital coupling of 8.97 cm^{-1} at the S_0/T_1 MECP is very small implying that the $T_1 \leftarrow S_1$ ISC is not allowed. Therefore, the energy and coupling calculations indicate that the probable multi-state mechanism is involved in the S_1 state, instead of the T_1 state. Having shown that the S_1 state probably is involved in the mechanism from the viewpoint of electronic energy and spin-orbital coupling, let us turn to the coupling between S_0 and S_1 . From group theory, although the $\tilde{A}^1A'' \leftarrow \tilde{X}^1A'$ transition of CH_2OO is not allowed, the situation of the complex $\text{CH}_2\text{OO} + \text{SO}_2$ system changes. Because the $\text{CH}_2\text{OO} + \text{SO}_2$ system has no special symmetry, that is in C_1 group, the vibronic coupling between the S_0 and S_1 states allows the $S_1 \leftarrow S_0$ internal conversion (IC) at the S_0/S_1 MECP. Therefore, IC might play an important role in the mechanism of the title reaction, instead of ISC.

Second, let us turn to the present PES, which is a prerequisite of the RPMD calculations. For simplicity, taking the most complicated transition part as an example, where $R(\text{S} - \text{O})$ and $R(\text{O} - \text{O})$ are not too large, individual and integration methods (further divided into Bayesian averaging and direct averaging) are adopted separately with the number of configurations ranging from 2000 to 16000, at intervals at 2000. Noting that the time complexity of GPR is $O(n^3)$, where n is the number of training points, if n points are broken into two equal parts then only around a quarter of former time is required in the GPR training process. Shown in Figure 3 is the descending trend of the fitting errors of GPR with the increase of point density, with a total of 2000 points as the validation set. From Figure 3, one can find that the errors steps down quickly at first with some fluctuation and then tends to be stabilized after reaching upon about 10000 points. As for the fitting methods, although individual fitting performs better than the other two, the superiority does not look obvious, especially compared with its shortcomings of expansive time consuming. In addition, there is little difference between the two integration methods, which indicates that in dynamics calculation, direct averaging is enough, sparing the bother of evaluating the uncertainties. Other regions of PES or different model structures reveal the similar rules, and for the sake of simplicity, their corresponding values are not shown one by one.

Third, based on the present GPR PES, the RPMD calculations were performed. Given in Table

II are present RPMD rate coefficient of $3.95 \times 10^{-11} \text{ cm}^3 \text{ molecule}^{-1} \text{ s}^{-1}$ as well as the previous experimental measurements [5, 6, 9–11] and computational results [12, 27]. In 2013 Sheps [5] employed multi-photon ultraviolet (UV) absorption and in 2015 Chhantyal-Pun *et al.* [11] used the UV CRDS. These measurements at room temperature give the rate coefficient in the range between 3.8×10^{-11} and 4.1×10^{-11} with the unit of $\text{cm}^3 \text{ molecule}^{-1} \text{ s}^{-1}$. This reaction was also investigated in pressure range between 50 and 450 Torr at room temperature by both Stone *et al.* [9] and Liu *et al.* [10], who reported pressure-independent rate coefficient in the range between $3.42 \times 10^{-11} \text{ cm}^3 \text{ molecule}^{-1} \text{ s}^{-1}$ and $3.53 \times 10^{-11} \text{ cm}^3 \text{ molecule}^{-1} \text{ s}^{-1}$. From Table II, a good agreement between the present RPMD rate coefficient and previously reported results can be found, which clearly shows the present calculations and statics mechanism are reasonable and accurate.

Fourth, Vereecken *et al.* [12] reported their statics mechanism at the M05-2X level in Figure 6 of reference [12]. They found an energy-optimal path with only one transition state (denoted by TSox in reference [12]) and a lowest barrier of $65.3 \text{ kcal mol}^{-1}$ (about 2.44 eV), and indicated in a dotted line of Figure 6 of reference [12]. Since the TSox wave function was found to be unstable towards breaking the alpha–beta spin electron symmetry at the M05-2X level, Vereecken *et al.* [12] proposed that TSox is a methodological artefact and this path is not a reaction pathway. In this work, however, we optimized the geometry of S_0/S_1 MECP, which is given in Table I and Figure 3 of the Supporting Information. A good agreement of geometries and energies of TSox and the S_0/S_1 MECP can be found, which implies that they are the same species. Because the previous M05-2X calculation [12] is single-reference, it cannot predict stable electronic wave function at MECP, making the previous M05-2X calculations not predict multi-state mechanism.

Finally, having shown the agreement among the present rate coefficient and the previous measurements [5, 6, 9–12, 27], let us turn to the dynamics mechanism, which has to be strictly studied through state-to-state quantum dynamics calculations. However, from the present statics mechanism, it is possible to predict the dynamics feature of the product group $\text{HCHO} + \text{SO}_3$, which implies probable experimental phenomenons. As shown in Figure 3 of the Supporting Information, the S_0/S_1 MECP has a structure of three-membered ring, which has a large internal tension force. This implies that it is easy to open the ring and form the product group, $\text{HCHO} + \text{SO}_3$. Considering that SO_3 is relatively heavy, the HCHO molecule should be in a rotationally excited state, which might be observed by quantum dynamics calculations. Thus, further high-dimensional quantum dynamics calculations for reactive probability is planned.

In summary, a multi-state statics mechanism of the $\text{CH}_2\text{OO} + \text{SO}_2 \rightarrow \text{HCHO} + \text{SO}_3$ reaction

was theoretically studied in a full quantum-mechanics fashion. Based on the present MCSCF and MRCI calculations, the statics mechanism involving the S_1 state was proposed, which is different from the previously proposed multi-state mechanism with a triplet state. [12] With this idea in the mind, extensive MRCI energy calculations were performed to build a database, based on which the PES was constructed through the GPR method. Further RPMD calculations on the present GPR PES predict the rate coefficient of $3.95 \times 10^{-11} \text{ cm}^3 \text{ molecule}^{-1} \text{ s}^{-1}$ at the room temperature, clearly agreeing with the previously reported values [5, 6, 9–12, 27]. The present MRCI calculations predict that the S_0/S_1 MECF has a three-membered ring, which has a large internal tension force. Therefore, the S_0/S_1 MECF is easy to open the ring and form the product group, HCHO + SO₃ with HCHO in its rotationally excited state. This phenomenon might be observed by state-to-state quantum dynamics theoretical and experimental observations.

See supplementary material document at <http://dx.doi.org/XXX>, where we give the numerical details in this work.

The authors gratefully acknowledge financial support by National Natural Science Foundation of China (Grant No. 21773186), Natural Science Foundation of Shaanxi Province (Grant No. 2019JM-380), Fundamental Research Funds for the Central Universities (Grant No. 3102017JC01001), and Hundred-Talent Program of Shaanxi.

-
- [1] O. Welz, J. D. Savee, D. L. Osborn, S. S. Vasu, C. J. Percival, D. E. Shallcross, and C. A. Taatjes. *Science* **335** (2012), 204–207.
 - [2] J. M. Beames, F. Liu, L. Lu, and M. I. Lester. *J. Am. Chem. Soc.* **134** (2012), 20045–20048.
 - [3] C. A. Taatjes, O. Welz, A. J. Eskola, J. D. Savee, A. M. Scheer, D. E. Shallcross, B. Rotavera, E. P. F. Lee, J. M. Dyke, D. K. W. Mok, D. L. Osborn, and C. J. Percival. *Science* **340** (2013), 177–180.
 - [4] Y.-T. Su, Y.-H. Huang, H. A. Witek, and Y.-P. Lee. *Science* **340** (2013), 174–176.
 - [5] L. Sheps. *J. Phys. Chem. Lett.* **4** (2013), 4201–4205.
 - [6] C. A. Taatjes, D. E. Shallcross, and C. J. Percival. *Phys. Chem. Chem. Phys.* **16** (2014), 1704–1718.
 - [7] J. Ahrens, P. T. M. Carlsson, N. Hertl, M. Olzmann, M. Pfeifle, J. L. Wolf, and T. Zeuch. *Angew. Chem. Int. Ed.* **53** (2014), 715–719.
 - [8] J. Kalinowski, M. Räsänen, P. Heinonen, I. Kilpeläinen, and R. B. Gerber. *Angew. Chem. Int. Ed.* **53** (2014), 265–268.

- [9] D. Stone, M. Blitz, L. Daubney, N. U. M. Howes, and P. Seakins. *Phys. Chem. Chem. Phys.* **16** (2014), 1139–1149.
- [10] Y. Liu, K. D. Bayes, and S. P. Sander. *J. Phys. Chem. A* **118** (2014), 741–747.
- [11] R. Chhantyal-Pun, A. Davey, D. E. Shallcross, C. J. Percival, and A. J. Orr-Ewing. *Phys. Chem. Chem. Phys.* **17** (2015), 3617–3626.
- [12] L. Vereecken, H. Harder, and A. Novelli. *Phys. Chem. Chem. Phys.* **14** (2012), 14682–14695.
- [13] I. R. Craig and D. E. Manolopoulos. *J. Chem. Phys.* **122** (2005), 084106.
- [14] I. R. Craig and D. E. Manolopoulos. *J. Chem. Phys.* **123** (2005), 034102.
- [15] R. Colleparado-Guevara, Y. V. Suleimanov, and D. E. Manolopoulos. *J. Chem. Phys.* **130** (2009), 174713.
- [16] A. Kamath, R. A. Vargas-Hernández, R. V. Krems, T. Carrington, and S. Manzhos. *J. Chem. Phys.* **148** (2018), 241702.
- [17] Q. Song, Q. Zhang, and Q. Meng. *J. Chem. Phys.* **152** (2020), 134309.
- [18] Q. Meng. *J. Phys. Chem. A* **122** (2018), 8320.
- [19] X. Lu, Q. Meng, X. Wang, B. Fu, and D. H. Zhang. *J. Chem. Phys.* **149** (2018), 174303.
- [20] Q. Meng and J. Chen. *J. Chem. Phys.* **150** (2019), 044307.
- [21] H.-J. Werner and P. J. Knowles. *J. Chem. Phys.* **82** (1985), 5053–5063.
- [22] P. J. Knowles and H.-J. Werner. *Chem. Phys. Lett.* **115** (1985), 259–267.
- [23] P. J. Knowles and N. C. Handy. *Chem. Phys. Lett.* **111** (1984), 315–321.
- [24] H.-J. Werner, P. J. Knowles, G. Knizia, F. R. Manby, and M. Schütz. *WIREs Comput. Mol. Sci.* **2** (2012), 242–253.
- [25] H.-J. Werner and P. J. Knowles. MOLPRO is a package of ab initio programs. Further information can be obtained from <http://www.molpro.net/>.
- [26] J. Hoeting, D. Madigan, A. Raftery, and C. Volinsky. *Stat. Sci.* **14** (1999), 382–401.
- [27] T. Kurtén, J. R. Lane, S. Jørgensen, and H. G. Kjaergaard. *J. Phys. Chem. A* **115** (2011), 8669–8681.

TABLE I: The MRCI optimized geometries (in Ångstrom and degree, for the atom notations see Figure 1) and energies (in eV) of the reactants (namely CH₂OO + SO₂), S_0/S_1 and S_0/T_1 MECPs, and products (namely HCHO + SO₃), together with the energy differences (in meV) for these MECPs. Geometries of the S_0/S_1 and S_0/T_1 MECPs are given in Figure 3 of the Supporting Information. Some important vibrational modes of the S_0 state along the reaction path and corresponding frequencies (in cm⁻¹) are also given. Finally, the spin-orbital coupling (in cm⁻¹) of the S_0/T_1 MECP is also given.

	Reactant	S_0/S_1	S_0/T_1	Product
<i>Geometry (in Ångstrom and degree) and Energy (in eV)</i>				
$R(S - O)$	∞^a	1.926	2.023	1.432
$R(O - O)$	1.350	1.829	3.204	∞^a
$R(C - O)$	1.275	1.175	1.180	1.206
$R(C - H)^b$	1.070	1.048	1.094	1.097
$R(C - H')^b$	1.070	1.076	1.094	1.097
$R(S - O')^c$	1.451	1.445	1.418	1.432
$R(S - O'')^c$	1.451	1.382	1.411	1.432
$A(C - O - O)$	118.0	67.9	152.7	—
$A(H - C - H)$	125.2	115.7	116.0	121.6
$A(O - C - H)^d$	117.4	123.5	122.0	119.2
$A(O - S - O')^d$	—	120.6	119.3	—
$A(O' - S - O'')$	118.6	126.0	120.4	120.0
E^e	0.00	2.20	8.10	-1.13
<i>Energy Difference (in meV) between Two States</i>				
MCSCF//MCSCF		9.05	5.40	
MRCI//MRCI		7.13	6.79	
<i>Imaginary Frequencies (in wavenumber)</i>				
O atom transition		237.4	451.4	
C - H symmetry stretch		824.2	335.6	
H - C - H bend		148.2	200.1	
C - H asymmetry stretch		412.5	139.9	
<i>Spin-orbital Coupling (in wavenumber)</i>				
	9		8.97	

- ^a In either reactant or product, the distance between two fragments is arbitrary large.
- ^b The H atom labels with and without apostrophe mean the different H atom of the system.
- ^c The O atom labels with apostrophe and double apostrophe mean those O atoms connected with the S atom.
- ^d Noting the expressions of $A(\text{O} - \text{C} - \text{H}') + A(\text{H} - \text{C} - \text{H}) + A(\text{O} - \text{C} - \text{H}) = 2\pi$ and $A(\text{O} - \text{S} - \text{O}'') + A(\text{O} - \text{S} - \text{O}') + A(\text{O}' - \text{S} - \text{O}'') = 2\pi$, one can obtain $A(\text{O} - \text{C} - \text{H}')$ and $A(\text{O} - \text{S} - \text{O}'')$ that are not given here.
- ^e Energy of MECP was computed by averaging the energies of the two states.

TABLE II: Comparison of rate coefficients of the $\text{CH}_2\text{OO} + \text{SO}_2 \rightarrow \text{HCHO} + \text{SO}_3$ reaction, obtained from the current work with previously reported values. The first column gives methods used in this work and previous experimental and theoretical work. The second column gives rate coefficients (in $\text{cm}^3 \text{ molecule}^{-1} \text{ s}^{-1}$). The third column represents some remarks of the rate coefficients, such as temperature, pressure, uncertainty, and so on. The rightmost column gives the authors and references.

Methods	Rate Coefficient	Remarks	Authors and Reference
<i>Calculations</i>			
RPMD@GPR/MRCI	3.95×10^{-11}	298 K, vacuum	This work
CCSD(T)//B3LYP	$\sim 4.0 \times 10^{-10}$	298 K, vacuum	Kurtén <i>et al.</i> [27]
M05-2X//CCSD(T)	$\sim 3.9 \times 10^{-11}$	298 K, vacuum	Vereecken <i>et al.</i> [12]
<i>Experiments</i>			
PIMS ^a	$(3.9 \pm 0.7) \times 10^{-11}$	298 K, 95% uncertainty	Welz <i>et al.</i> [1]
multi-photon UV	$(4.1 \pm 0.3) \times 10^{-11}$	295 K, 95% uncertainty	Sheps [5]
LIF/PIMS ^a	$(3.42 \pm 0.42) \times 10^{-11}$	295 K, 1.5 ~ 450 Torr	Stone <i>et al.</i> [9]
LIF ^a	$(3.53 \pm 0.29) \times 10^{-11}$	(295 \pm 2) K, 50 ~ 200 Torr	Liu <i>et al.</i> [10]
CRDS ^b	$(3.80 \pm 0.04) \times 10^{-11}$	293 K, 7 ~ 30 Torr	Chhantyal-Pun <i>et al.</i> [11]

^a LIF means laser-induced fluorescence spectroscopy and PIMS means photoionisation mass spectrometry.

^b CRDS means cavity ring-down spectroscopy.

Figure 1: The schematic diagram of the coordinate constructed consisting of bond lengths, bond angles and dihedral angles. The CH_2OO molecule constructs a plane, while the SO_2 molecule constructs another plane. These two plans are shown by different colors. Giving all of atom labels, We also show some important geometry parameters, including $R(\text{S} - \text{O})$, $R(\text{O} - \text{O})$, $R(\text{C} - \text{O})$. For clarity, the bond angles and dihedral angles are not shown here. They are defined by the standard geometry of molecule.

Figure 2: Electronic potential energy profile (in Hartree) of the $\text{CH}_2\text{OO} + \text{SO}_2$ reaction obtained at the MRCI/aug-cc-pVTZ level. The black, red, and blue curves represent the PECs of the S_0 , S_1 , and T_1 states, respectively. As shown in Table I, the $R(\text{S} - \text{O})$ values of the S_0/S_1 and S_0/T_1 MECPs are 1.926 Å and 1.998 Å, respectively, which are indicated here by a gray box.

Figure 3: The graph of error varying with the training datasets ranging from 2000 to 16000. On the vertical axis is number of data points, growing from top to bottom at fixed intervals, and on the horizontal axis is the test error (in Hartree). Each horizontal line is centered at the markers, pentagram or rhombus, stretching out a standard error on both sides. As the legend shows, different markers represent different methods and different colors of pentagram mean distinct integration models. Every method takes on the same trend, with errors descending fast at first and then stable. At the same time of error reducing, the gap among the three methods shrinks based on the same data amounts.

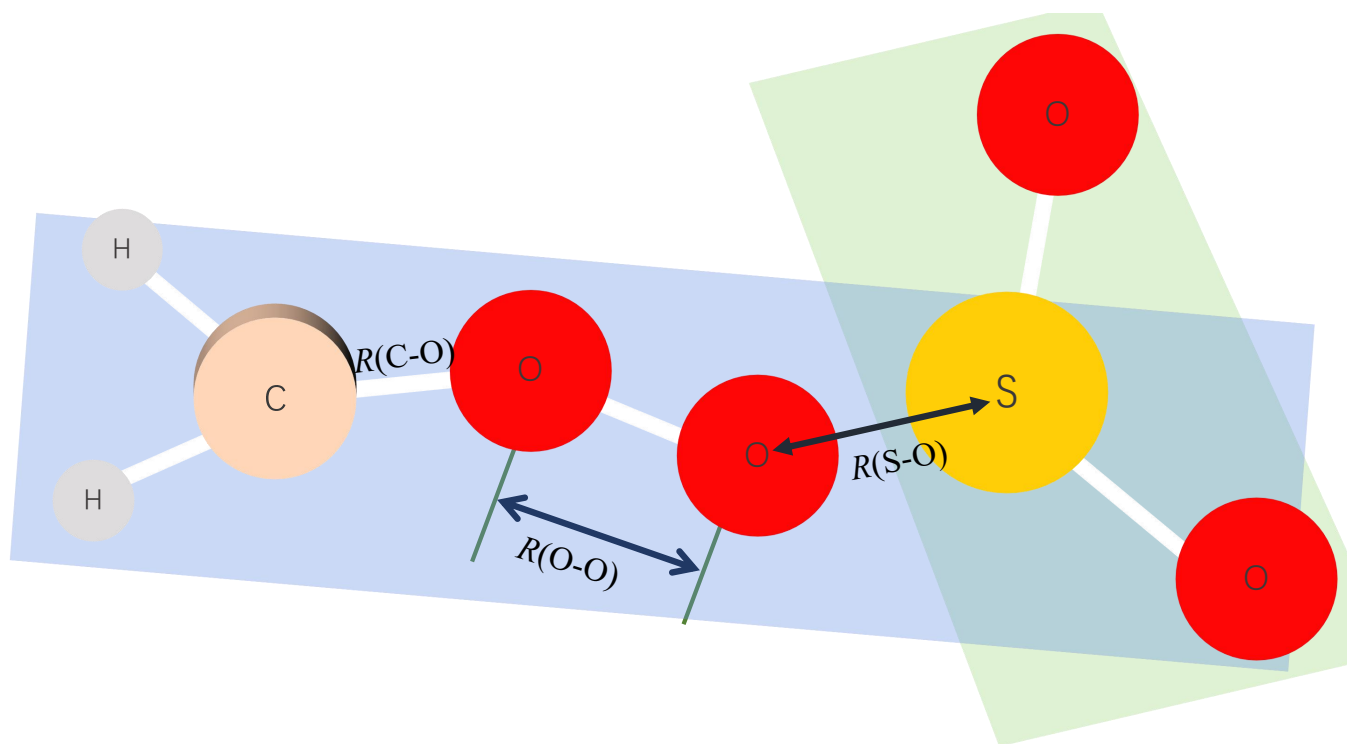


FIG. 1: Mechanism, PES+Rate, CH₂OO+SO₂

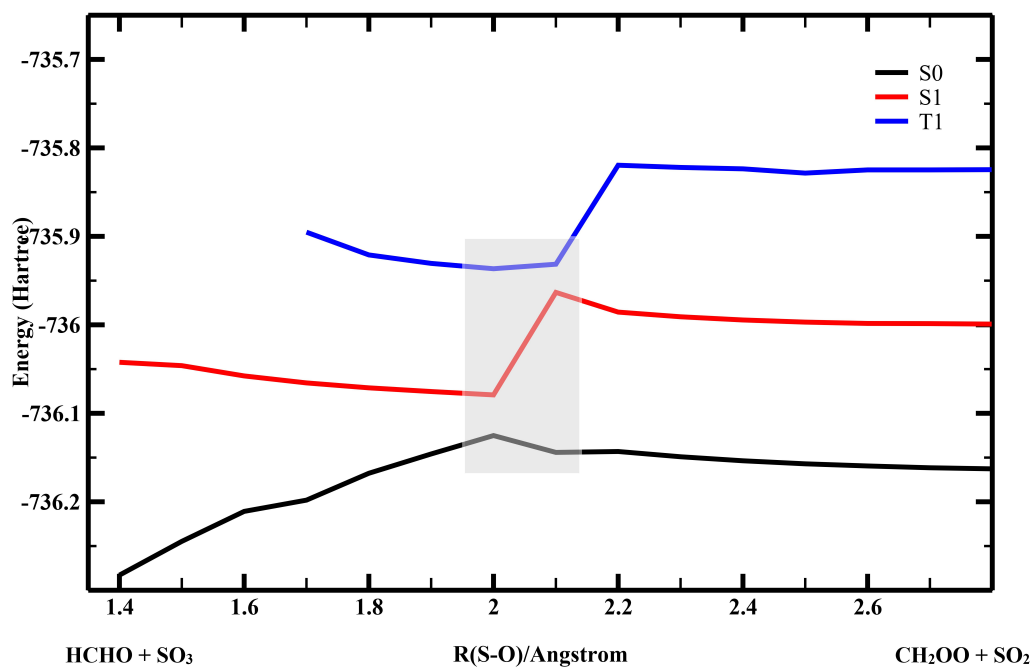


FIG. 2: Mechanism, PES+Rate, $\text{CH}_2\text{OO} + \text{SO}_2$

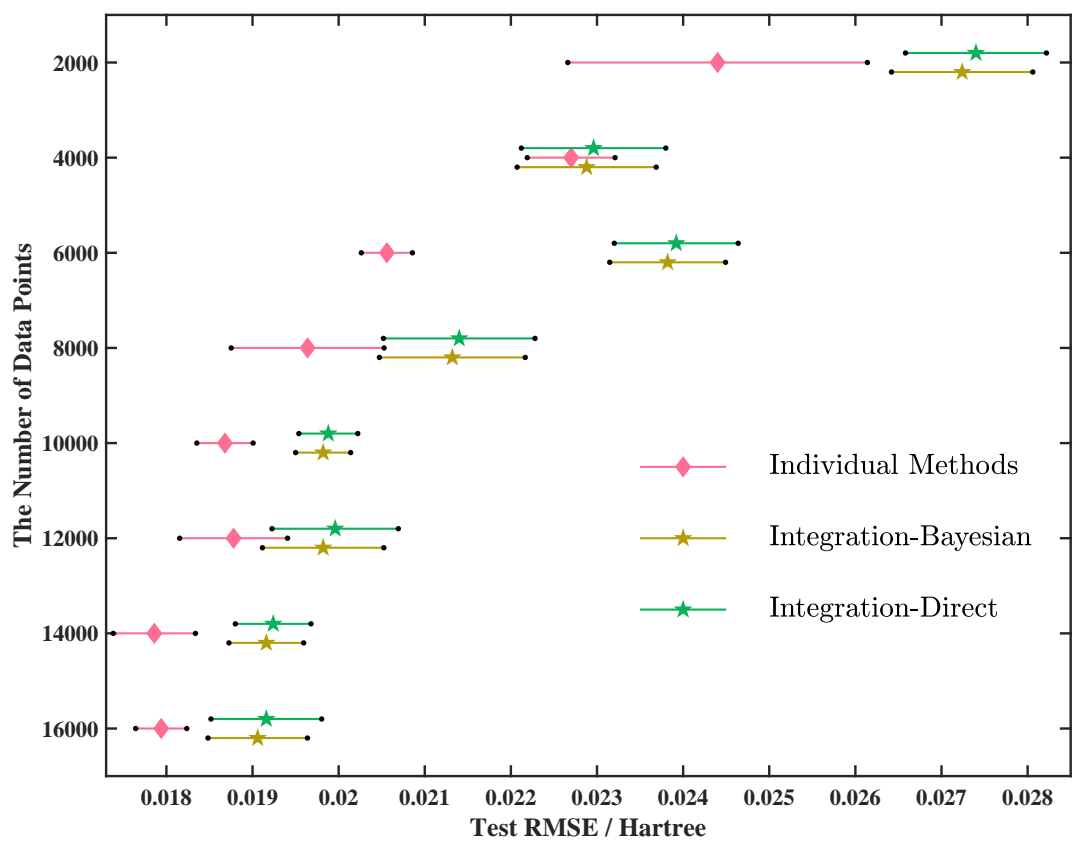


FIG. 3: Mechanism, PES+Rate, CH₂OO+SO₂